



Cite this: DOI: 10.1039/d4ta06642a

p–d Orbital coupling in silicon-based dual-atom catalysts for enhanced CO₂ reduction: insight into electron regulation of active center and coordination atoms†

Meijie Wang,^a Yaowei Xiang,^a Yuxing Lin,^a Yang Sun,^a Zi-zhong Zhu,^a Shunqing Wu^a and Xinrui Cao^{*ab}

Transition metal (TM) dual-atom catalysts (DACs) show promise for carbon dioxide reduction reaction (CO₂RR) through d–d orbital cooperative interactions, but their effectiveness is often curtailed by the linear scaling relations between *CO and *CHO on transition metal sites, typically resulting in CO as the predominant product. Specifically, the p–d orbital coupling may exert further influence to regulate the electronic properties and catalytic activity of DACs, which will be of great significance for promoting CO₂RR. Herein, we combine density functional theory (DFT) and machine learning (ML) to investigate the potential of heteronuclear DACs with the Si-TM dual-atom active sites in CO₂RR and evaluate the influence of the coordination environment. Among 27 SiTMN₆ and 336 SiTMN₅An (A = B, C, and n represents position) DACs, three SiTMN₆ and six SiTMN₅An DACs demonstrate high activity and selectivity in converting CO₂ to CH₄ or CH₃OH. The p_z band distribution (ϵ'_{p_z}), influenced by both p–d orbital coupling and the coordinating environment, has been elucidated. The optimal ϵ'_{p_z} results in superior reaction activity by facilitating optimal adsorption effects for reaction intermediates. This work not only provides comprehensive understanding of reaction mechanisms for CO₂ reduction on silicon-based dual-atom catalysts, but also reveals the irreplaceable role of p–d coupling in the performance regulation of DACs. With this knowledge and the aid of machine learning, we establish fundamental principles and descriptors for the accelerated discovery of efficient dual-atom catalysts.

Received 18th September 2024
Accepted 28th October 2024

DOI: 10.1039/d4ta06642a

rsc.li/materials-a

1 Introduction

Efficient conversion and optimal utilization of carbon dioxide (CO₂) are critical for advancing a sustainable and carbon-neutral economy.^{1–3} Electrocatalytic reduction has emerged as a prominent approach for converting CO₂ into valuable green fuels, such as carbon monoxide (CO), formic acid (HCOOH), formaldehyde (CH₂O), methanol (CH₃OH), methane (CH₄), and ethylene (C₂H₄), thereby achieving carbon neutrality in a closed-loop system.^{4–6} Despite its potential, the commercialization of electrocatalytic CO₂ reduction (CO₂RR) is hindered by challenges associated with existing catalysts.

Recently, a variety of single-atom catalysts (SACs) composed of non-precious metals have been identified as promising candidates for the CO₂RR.⁶ These SACs, particularly those N-doped graphene-supported single transition metal atoms (M–N–C, M =

Fe,⁷ Co,⁸ Ni,⁹ Mn,¹⁰ etc.), are notable for their 100% active atom utilization, relatively high activity and selectivity, and the tunability of the active center microenvironment.^{11–13} However, the chemical inertness of CO₂ with the highest oxidation state of carbon, attributable to the extremely high thermal stability and the nonpolarity, results in physical adsorption and quite weak activation at the single atom site.^{14–16} Furthermore, the electrocatalytic activation and deep reduction of CO₂ through proton-coupled electron transfers are constrained by kinetic limitations, with CO often being the primary product of SACs for CO₂RR. Dual-atom catalysts (DACs), not only possess the advantages of SACs but also allow the enhancement of inert molecule activation and the optimization of multi-electron transfer pathways,^{12,17–19} owing to their synergistic interactions, which positions them as promising candidates for advancing CO₂RR technology. Extensive experimental^{20–29} and theoretical^{30–33} investigations show that DACs incorporating d-block metal atoms have enhanced electrocatalytic performance due to d–d orbital interactions. However, the range of products is predominantly limited to few-electron transfer species CO. While some DACs show potential for facilitating multi-electron transfer reactions, their broader applicability is still restricted by the linear scaling

^aDepartment of Physics, Xiamen University, Xiamen 361005, China. E-mail: xinruicao@xmu.edu.cn

^bFujian Provincial Key Laboratory of Theoretical and Computational Chemistry, Xiamen University, Xiamen 361005, China

† Electronic supplementary information (ESI) available. See DOI: <https://doi.org/10.1039/d4ta06642a>

relations between *CO and *CHO on transition metal sites. This inherently limits the further reduction of CO, posing a significant challenge for achieving multi-electron transfer products.^{30–33}

The strategic incorporation of p-block atoms and transition metal atoms has revealed remarkable effects on electronic properties and catalytic activities due to p–d orbital coupling.³⁴ Most of the previous researches on the p–d orbital coupling primarily focused on introducing nonmetal heteroatoms (*e.g.*, B, C, N, *etc.*) as coordination atoms to regulate the electronic structure of the active atoms, yet it fails to provide a synergistic site. Actually, p-block elements such as Al, Ga, Ge,³⁵ Si,^{36,37} and Sn³⁸ not only modulate the local coordination environment and the d-band distribution of the transition metal centers but also jointly assume as the role of the active site. When bonded to d-block metals for CO₂RR, they can optimize the adsorption strength of reaction intermediates and facilitate the reaction. Specifically, the Cu–Si direct bonding in the core–shell structured Cu–SiO₂ catalyst makes the nearby bare Cu sites with large charge density, and these bare Cu sites and the Si–O–H sites are conducive to stabilizing the *CHO intermediate on the Cu–Si interface, thus enhancing the selectivity for converting CO₂ into multi-electron transfer and multicarbon products.³⁶ In addition, experimental work by Kim *et al.* has characterized SiFe sites loaded on N-doped graphene, which exhibited high oxygen reduction reaction (ORR) activity.³⁹ Based on these insights, our prior research has focused on DACs with the SiFeN₆ configuration for CO₂RR, where the Si–Fe centers significantly enhance the adsorption and activation of *CO₂, facilitating its selective reduction to CH₄.³⁷ This preliminarily demonstrates the potential of SiFeN₆ DACs for electrocatalytic CO₂RR. In addition, the influence of changes in the coordination environment on catalytic activity is significant.^{40–49} However, to the best of our knowledge, there remains a lack of systematic studies focused on screening and designing SiTM DACs that incorporate various transition metal atoms and coordination environments. Given the many possible combinations of heteronuclear dimers and coordination environment, as well as the currently many unexplored DACs in the experiment, it is imperative to establish a feasible strategy, by which we could elucidate the fundamental factors that enhance CO₂RR, thereby facilitating the rational design of promising candidates with much improved CO₂RR activity.

In this work, utilizing density functional theory (DFT) calculations and machine learning (ML), we systematically investigate the CO₂RR performance of heteronuclear 27 SiTMN₆ DACs and 336 SiTMN₅An DACs, where A is either Boron or Carbon, indicating B or C substitution for the N atom closest to the Si and TM atoms, the positions of different N atoms are labeled by n embedded on a two-dimensional N-doped graphene surface. We successfully screened out three SiTMN₆ and six SiTMN₅An DACs with high activity and selectivity in converting CO₂ to CH₄ or CH₃OH. The p_z band distribution (ϵ'_{p_z}), influenced by both p–d orbital coupling and the coordinating environment, have been elucidated. The optimal ϵ'_{p_z} results in superior reaction activity by facilitating optimal adsorption effects for reaction intermediates. A detailed analysis of the reaction activity and electronic structure of these DACs enables us to suggest a universal strategy for designing high-performance CO₂RR catalysts. This proposed

strategy serves as a guiding framework for further exploration of various DACs compositions, with the goal of improving their applicability in diverse electrocatalytic reactions.

2 Computational details

We use the Vienna *Ab initio* Simulation Package (VASP) based on spin-polarized density functional theory^{50,51} for the generation of self-consistent relaxed geometric optimization. The projector augmented-wave (PAW) method was used to describe the ion–electron interaction.⁵² The Perdew–Burke–Ernzerhof (PBE) generalized gradient approximation (GGA) was used to describe exchange–correlation.⁵³ The DFT-D3 method was used to evaluate van der Waals interactions between the substrates and adsorbates.^{54,55} The plane wave energy cutoff was set as 500 eV. The Brillouin-zone integration was performed using a $3 \times 3 \times 1$ *k*-point mesh for geometric optimization and a $9 \times 9 \times 1$ *k*-point mesh for electronic property calculations. The electronic energy and forces were converged to 1.0×10^{-5} eV Å⁻¹ and 0.02 eV Å⁻¹, respectively. The VASPKIT code⁵⁶ was used to post-process the VASP calculated data.

To take into account the effects of solvation and applied potentials on the reaction free energies, we continue to optimize the structure obtained from the VASP calculations using the open-source plane-wave DFT software JDFTx.⁵⁷ The free energy of the reaction intermediates was calculated using the constant potential method (CPM), and the applied potential is set to 0 V. The solvation effect was considered using the CANDEL model.⁵⁸ All calculations were modeled using Perdew–Burke–Ernzerhof (PBE) functional⁵³ and GBRV 1.5 pseudopotentials,⁵⁹ considering an electronic planewave cutoff of 20 hartree and charge density cutoff of 100 hartree. The van der Waals interactions between the substrates and adsorbates were evaluated using the DFT-D3 method.^{54,55} The Brillouin-zone integration was performed using a $3 \times 3 \times 1$ *k*-point mesh for geometric optimization and electronic property calculations. The convergence criteria of electronic energies were set to 1×10^{-5} eV (3.67493×10^{-7} hartree) and 1×10^{-6} eV (3.67493×10^{-8} hartree) for geometric optimization and electronic property calculations, respectively.

The free energy change of each fundamental step was calculated by⁵⁸

$$\Delta G_{\text{CPM}} = G(I_2) - G(I_1) - G(\text{H}_2(\text{g}))/2 + |e|U - (q_1 - q_2)\mu_e \quad (1)$$

where the $G(I_1)$ and $G(I_2)$ donate the free energies of the reactants and products at corresponding potentials, and the $G(\text{H}_2(\text{g}))/2$ is the free energy of the hydrogen. The U is the applied potential *versus* reversible hydrogen electrode (RHE). Also, q_1 and q_2 represent the total net charges of reactants and products, respectively. And the μ_e is the electron energy determined by the electrode potential.

The formation energy (E_f) of SiTM dimer embedded N-doped graphene is calculated as

$$E_f = \frac{1}{2} (E_{\text{SiTMN}_6} - E_{\text{V}_4\text{N}_6} - E_{\text{Si}} - E_{\text{TM}}) \quad (2)$$

The meaning of 1/2 represents the average formation energy of Si and TM atoms embedded in V₄N₆-graphene (V: vacancy,

and N: nitrogen). E_{Si} and E_{TM} are the DFT energy of Si and TM atoms in their most stable bulk structures, respectively. $E_{\text{V}_4\text{N}_6}$ is the DFT energy of N-doped graphene framework with four vacant sites. E_{SiTMN_6} is the DFT energy of SiTMN₆ DACs.

The dissolution potential $U_{\text{diss}}(\text{TM})$ are defined as,

$$U_{\text{diss}}(\text{TM}) = U_{\text{diss}}^{\circ}(\text{TM, bulk}) - \frac{E_{\text{SiTMN}_5\text{An}} - E_{\text{SiV}_2\text{N}_5\text{An}} - E_{\text{TM}}}{ne} \quad (3)$$

where $U_{\text{diss}}^{\circ}(\text{TM, bulk})$ are the standard dissolution potential of TM bulk. And n is the number of electrons involved in the TM bulk dissolution process. $E_{\text{SiV}_2\text{N}_5\text{An}}$ is the DFT energy of SiTMN₅An without TM atom. E_{TM} is the DFT energy of TM atom in its most stable bulk structure.⁶⁰

Furthermore, in our machine learning (ML) analysis, we employed Gradient Boosted Regression⁶¹ (GBR) models to predict the adsorption free energies (ΔG_{CO_2} and ΔG_{OH}). To evaluate the performance of the model, a fivefold cross-validation was performed on the training dataset. The data was split into training and test sets with a ratio of 8 : 2. Additional details regarding feature selection, algorithm selection, and model training regimes can be found in the ESI.†

3 Results and discussions

3.1 Research framework for SiTM DACs

This study utilizes a combined approach of DFT calculations and ML techniques to enhance the understanding and optimization of SiTMN₆ and SiTMN₅An DACs for CO₂RR, as illustrated in Fig. 1. Firstly, we constructed 28 heteronuclear SiTMN₆ DACs using

different combinations of TM atoms and Si atom, with the TM atoms ranging from 3d, 4d and 5d transition metals from IIIB to IIB (except Hg). DFT calculations were then performed to assess the comprehensive performance of CO₂RR on these aforementioned SiTMN₆ DACs, and the corresponding activity descriptors were also explored. In order to optimize the catalytic performance of SiTM DACs and verify the universality of reaction activity descriptions, a catalytic space with 336 catalysts is constructed by exploring the diversity of SiTMN₅An DACs by considering B and C substitutions in the N₆ coordination environment. Currently, machine learning is widely used to accelerate the acquisition of new material properties in a vast chemical space.^{62–68} Herein, we used the adsorption Gibbs free energies of CO₂ (ΔG_{CO_2}) and *OH (ΔG_{OH}) of the SiTMN₅An DACs as a proxy. Utilizing the scikit-learn⁶⁹ library, several combinations of feature selection, algorithm selection, and model training regimes were systematically explored to determine the optimal model (for detail discussions, see ESI†). Next, the optimal trained ML model was applied to predict ΔG_{CO_2} and ΔG_{OH} of the SiTMN₅An DACs. After that, we performed high-throughput screening of these catalysts. This screening process led to the identification of six exemplary catalysts for CO₂RR, verifying the effectiveness of our proposed descriptor in guiding the optimization of catalysts.

3.2 Structure and stability of SiTM₆ DACs

Previous theoretical investigations demonstrated that TM dimers embedded graphene with six doped N atoms and four carbon vacant sites (V_4N_6 -graphene; V: vacancy, and N:

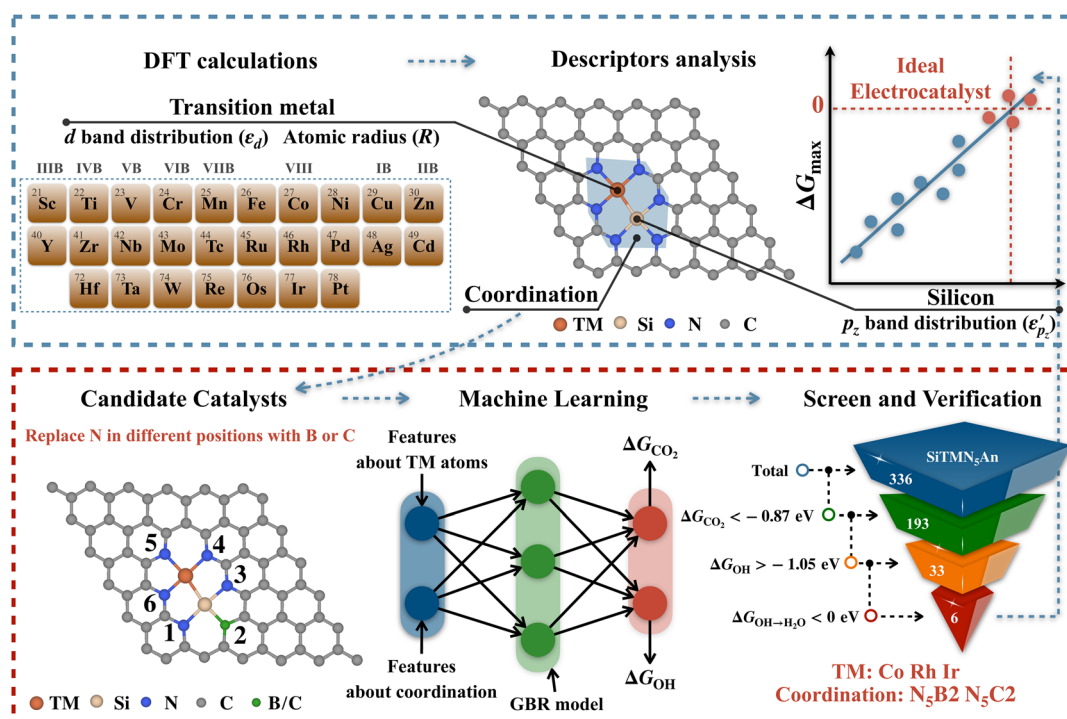


Fig. 1 Illustration of our research framework. The blue dashed box describes the comprehensive evaluation of the CO₂RR performance of SiTMN₆ DACs, identifying catalytic activity descriptors (ΔG_{max}). The red dashed box outlines the construction of a new catalyst space through coordination replacing in the N₆ coordination environment with B and C, and the screening process based on ML results, ultimately screening optimal catalysts and verifying the universality of our proposed descriptors in predicting and enhancing catalytic performance.

nitrogen) is the most energetically favorable configuration. Additionally, a range of advanced characterization techniques have conclusively verified the presence of atomically dispersed dual-atom TM pair sites on N-doped graphene.^{28,29} Accordingly, these constructed SiTMN₆ DACs are based on this binding. As displayed in Fig. 1, the Si and TM atoms in DACs are bonded and both surrounded by three pyridine sp²-N atoms. The calculated Si–TM bond lengths are in the range of 2.24 Å to 2.90 Å (Fig. 2(a)). Obviously, the bond lengths between Si and TM

atoms initially decrease and then increase from left to right across the same period. Additionally, it is important to note that different transition metal atoms influence the geometric configuration of SiTM atomic pairs. As illustrated in Fig. S5 and S6(a),† only SiTMN₆ DACs featuring TM atoms such as Mn, Fe, Co, Ni, Pd, and Pt maintain nearly planar geometries. In contrast, other TM atoms lead to the protrusion of Si atoms from the graphene plane. When the degree of protrusion is relatively mild, Si continues to bond with three nitrogen atoms

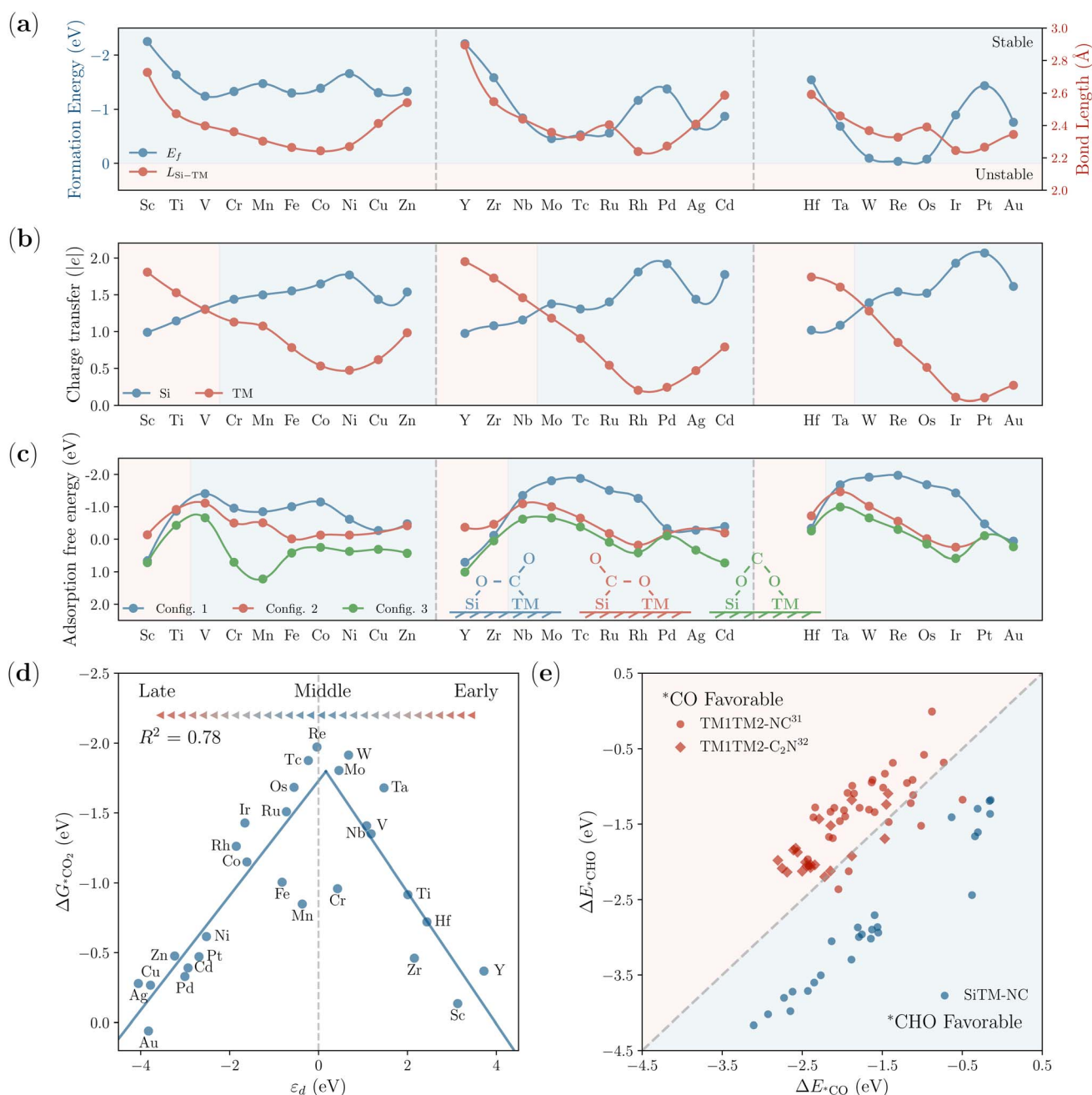


Fig. 2 (a) The formation energies and bond length between Si atoms and TM atoms on different SiTMN₆ DACs; (b) The charge transfer of Si atoms and TM atoms on different SiTMN₆ DACs; (c) The adsorption free energies of different CO₂ adsorption configuration on SiTMN₆ DACs. Partial data missing represents no stable adsorption structure; (d) relationship of ϵ_d and $\Delta G^*_{\text{CO}_2}$; (e) ΔE^*_{CHO} and ΔE^*_{CO} on different SiTMN₆-NC, TM1TM2N₆-NC³¹ and TM1TM2-C₂N³² DACs. For clarity and simplicity in the figures, SiTMN₆ is abbreviated as TM, as same below.

($N_c = 3$). For transition metals with larger radius, the protrusions are more distinct, leading to the rupture of the bond between Si and the nitrogen atom at position 3 with the corresponding distances are larger than 2.2 Å, as depicted in Fig. S7.† Accordingly, the Si bonds with only two nitrogen atoms ($N_c = 2$) and the TM typically remains coordinated with three or four nitrogen atoms, as detailed in Fig. S6(b and c).† Furthermore, the heatmap in Fig. S6(d)† displays SiTMN₆ structures with various transition metals, indicating that most early and early-middle transition metals exhibit $N_c = 2$, whereas most late-middle and late transition metals show $N_c = 3$. Moreover, the formation energies (E_f) of these 28 SiTMN₆ configurations were all negative, ranging from -2.25 to -0.04 eV, indicating their thermodynamic stability, as shown in Fig. 2(a).

The Bader charge analyses were used to study the electron transfer features of SiTMN₆ DACs. As shown in Fig. 2(b), the results revealed that both Si and TM atoms donate electrons to N-doped graphene. The charge transfer quantity of Si atoms initially increases and then decreases from left to right across the same period, while the TM atoms show the opposite trend. For early TM atoms, the TM atoms exhibited a higher positive charge compared to Si atoms. However, in configurations involving middle to late transition metals, the charge distribution reversed, with Si atoms carrying more positive charge. This charge analysis indicates that the incorporation of Si improves the adsorption and activation of negatively charged reactants, such as *OH and O atom in *CO₂ or *CHO, relative to traditional TM DACs. This advantage is particularly notable when Si is combined with TM atoms in the middle and later stages of the periodic table.

Next, we focus on the adsorption and activation of CO₂, which are crucial for CO₂RR. We analyzed three primary adsorption configurations, as depicted in Fig. 2(c). The Si-O-TM-C bonding configuration (Config. 1) was found to be the most energetically favorable for most SiTMN₆ DACs, attributed to the higher positive charge on Si. In contrast, for early TM SiTMN₆ DACs (TM = Sc, Y, Ti, Zr, Hf), where TM atoms carry a more significant positive charge, the Si-C-TM-O bonding configuration (Config. 2) was preferred. The Si-O-C-TM-O configuration (Config. 3) consistently showed the least energetic favorability across all structures. Notably, we observed distinct adsorption capabilities for CO₂ among the early, middle, and late TM atoms, displaying a clear volcano relationship. Middle TM atoms exhibited the highest CO₂ adsorption capability, while early and late TM atoms both showed comparatively weaker ability to bind CO₂. To elucidate the origin of the difference, we calculated the partial density of states (PDOS) for the molecule-substrate systems. As illustrated in Fig. S8(b)† for SiMoN₆ DACs, before adsorption, the Mo 4d orbitals are localized near the Fermi level, with a semi-empty and semi-full d orbitals, which facilitate electron donation to the lowest unoccupied molecular orbital (LUMO) of CO₂ and electron acceptance from the CO₂ highest occupied molecular orbital (HOMO). After adsorption, the occupied CO₂ 1π_g orbitals donate electrons to the Mo 4d orbitals, while the Mo 4d orbitals back-donate electrons to the antibonding 2π_u orbitals of the CO₂ molecule. As shown in Fig. S8(a) and (c),† compared to the

Mo 4d orbitals, the 4d orbitals of Nb shift upward, and the 4d orbitals of Rh shift downward. These shifts both weaken the electronic interaction between SiTM dual-atom center and CO₂. This trend correlates with the ϵ_d , as detailed in Fig. 2(a). When the ϵ_d is distant from the Fermi level, the interaction between the transition metal and the adsorbed molecules is weak, resulting in weaker adsorption. It is noteworthy that Si atoms enhance the adsorption and activity of CO₂ by the p-d coupling. As illustrated in Fig. S9(a),† we observed significant p-d coupling interactions between Si 3p and Fe 3d orbitals. Compared to the Fe₂N₆ DACs (S9(b)†), the p-electrons in Si are more spatially delocalized than the d-electrons in TM atoms, facilitating more effective electron interactions with the orbitals of CO₂ molecule at deeper energy levels. Additionally, the increased positive charge on Si in SiTM configurations further enhances their adsorption and activation capabilities for CO₂ compared to homonuclear transition metal atoms DACs.³⁷

Previous theoretical studies have identified that the supported TM dimer catalysts are limited by a linear scaling relationship between the adsorption energies of *CO and *CHO intermediates.^{31,32} This scaling relationship has been a significant hindrance, preventing the efficient reduction of *CO to *CHO, and thereby limiting the conversion of CO₂ to multi-electron transfer products such as CH₃OH and CH₄. Our findings, as depicted in Fig. 2(b), suggest that the incorporation of Si atoms into the SiTMN₆ structures maintains the linear scaling relationship. However, it enhances the stabilization of the *CHO intermediate. This stabilization is crucial as it facilitates the transition from *CO to *CHO. As shown in Fig. S10,† similar to the adsorption of CO₂, the p-electrons in silicon are more spatially delocalized compared to the d-electrons in transition metals. Such delocalization enhances the efficiency of electron interactions with the orbitals of the O atom in *CHO. Consequently, SiTMN₆ dual-atom catalysts exhibit the potential to effectively reduce CO₂ to multi-electron transfer products.

3.3 CO₂RR pathways and activities of SiTM₆ DACs

To evaluate the CO₂RR performance of different SiTM DACs, the Gibbs free energy profiles of SiTM DACs systems based on C₁ product pathways were systematically explored. Due to the inability of SiAuN₆ to capture CO₂ ($\Delta G_{*CO_2} > 0$ eV), we will not conduct a systematic study on it. Fig. 3(a) summarizes the optimal CO₂RR pathways across all SiTMN₆ structures, with detailed free energy step diagrams provided in Fig. S11–S20.† Additionally, Table S3† presents the products, ΔG_{max} , and Potential-determining Steps (PDS) for all structures.

Our research elucidates distinct reaction pathways for SiTMN₆ DACs, varying with the type of TM atoms utilized. Note that the Si-TM DACs have comparable activity for early and middle TM atoms, where Si and TM catalyze different reaction intermediates. Conversely, in DAC systems with late TM atoms, TM atoms exhibit weak catalytic activity. The reaction intermediates are mainly adsorbed on the top position of Si.

In systems doped with early transition metals (Sc, Y, Ti, Zr, Hf), CO₂ initially undergoes hydrogenation to form the *OCHO intermediate, as depicted in Fig. 3(a). During this process, Si-O

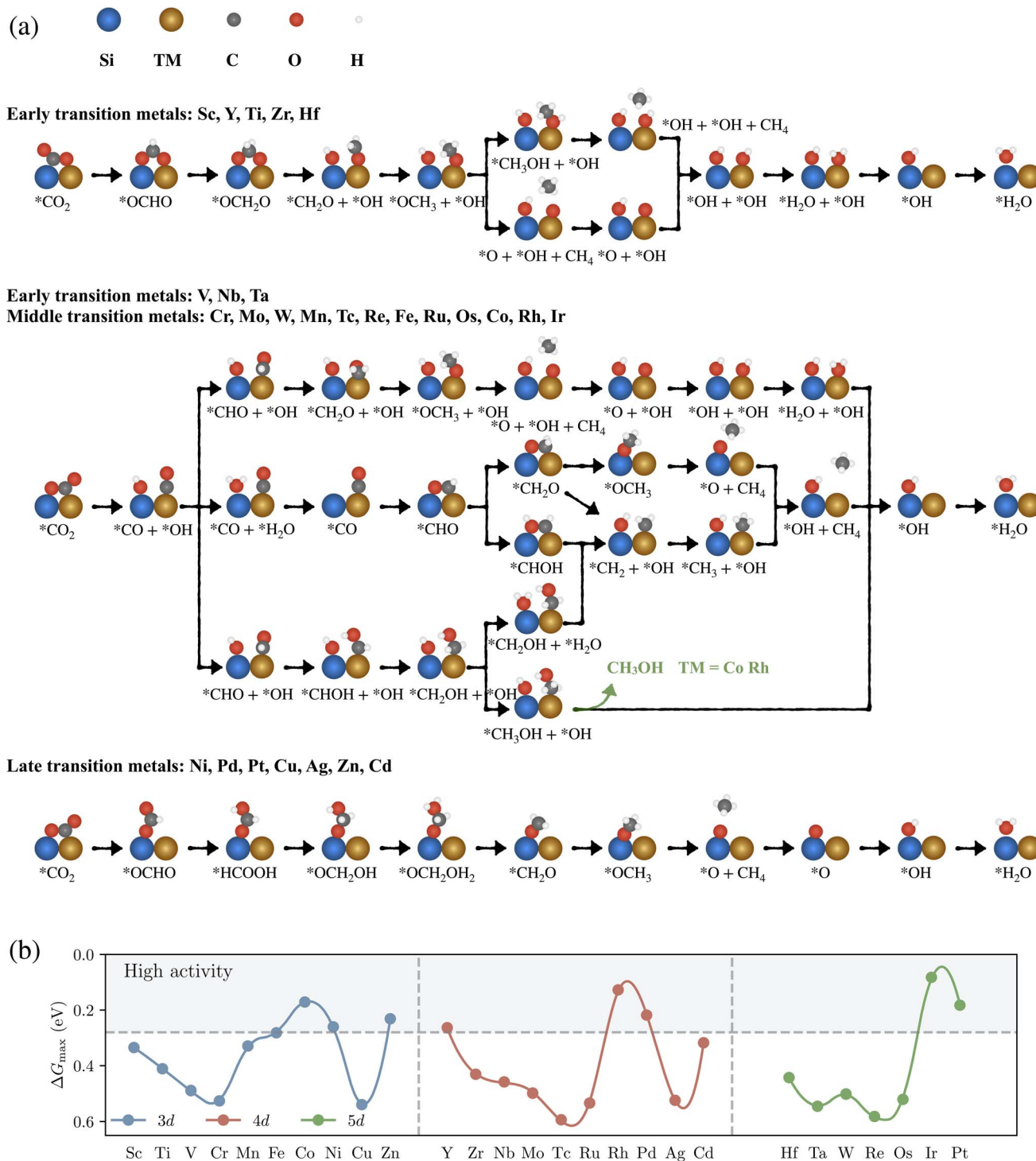


Fig. 3 (a) Reaction pathways for CO₂RR on SiTMN₆ DACs; (b) the computed ΔG_{\max} of SiTMN₆ DACs for CO₂RR.

and TM–O bonds form, which are subsequently hydrogenated to $^*\text{OCH}_2\text{O}$. This intermediate preferentially dissociates into $^*\text{OH}$ and $^*\text{CH}_2\text{O}$. Further, $^*\text{CH}_2\text{O}$ undergoes a series of reduction reactions on TM atoms (Sc, Y), leading to CH₄ through the pathway $^*\text{CH}_2\text{O} \rightarrow ^*\text{OCH}_3 \rightarrow ^*\text{CH}_3\text{OH} \rightarrow ^*\text{OH} + \text{CH}_4$. Alternatively, on TM atoms (Ti, Zr, Hf), $^*\text{CH}_2\text{O}$ is reduced to CH₄ via the pathway $^*\text{CH}_2\text{O} \rightarrow ^*\text{OCH}_3 \rightarrow ^*\text{O} + \text{CH}_4$. Subsequently, $^*\text{OH}$

is hydrogenated to $^*\text{H}_2\text{O}$, followed by $^*\text{H}_2\text{O}$ desorption. In the case of $^*\text{O}$, it is firstly hydrogenated to form $^*\text{OH}$, and then further hydrogenated to $^*\text{H}_2\text{O}$.

In SiTMN₆ DAC systems doped with early transition metals (V, Nb, Ta) and middle transition metals (Cr, Mo, W, Mn, Tc, Re, Fe, Ru, Os, Co, Rh, Ir), a preference is observed for dissociated $^*\text{CO} + ^*\text{OH}$ intermediates, with $^*\text{CO}$ adsorbed on TM and $^*\text{OH}$

on Si. This preference is attributed to the proximity of the intermediate transition metal d electrons to the Fermi level, which strongly activates CO_2 and weakens the C–O bond. In systems containing early transition metals (V, Nb, Ta), *CO is preferentially reduced to CH_4 , following the sequence $\text{*CO} \rightarrow \text{*CHO} \rightarrow \text{*CH}_2\text{O} \rightarrow \text{*OCH}_3 \rightarrow \text{*O} + \text{CH}_4$. Subsequently, two *OH groups are coupled to form $\text{*H}_2\text{O}$, and then the desorption of $\text{*H}_2\text{O}$ followed. For systems with middle transition metals (Cr, Mo, W, Mn, Tc, Re, Fe, Ru, Os), the primary process involves the hydrogenation of *OH groups to $\text{*H}_2\text{O}$, and then $\text{*H}_2\text{O}$ is desorbed. This is followed by the reduction of *CO to CH_4 via the following pathways: (i) For Fe and Ru: $\text{*CO} \rightarrow \text{*CHO} \rightarrow \text{*CH}_2\text{O} \rightarrow \text{*OCH}_3 \rightarrow \text{*O} + \text{CH}_4$; (ii) For Cr, Mn, Tc: $\text{*CO} \rightarrow \text{*CHO} \rightarrow \text{*CH}_2\text{O} \rightarrow \text{*CH}_2 + \text{*OH} \rightarrow \text{*CH}_3 + \text{*OH} \rightarrow \text{*OH} + \text{CH}_4$; (iii) For Mo, W, Re, Os: $\text{*CO} \rightarrow \text{*CHO} \rightarrow \text{*CHOH} \rightarrow \text{*CH}_2 + \text{*OH} \rightarrow \text{*CH}_3 + \text{*OH} \rightarrow \text{*OH} + \text{CH}_4$. In systems with Co and Rh, *CO is preferentially reduced to $\text{*CH}_3\text{OH}$ through the pathway $\text{*CO} \rightarrow \text{*CHO} \rightarrow \text{*CHOH} \rightarrow \text{*CH}_2\text{OH} \rightarrow \text{*CH}_3\text{OH}$, followed by hydrogenation of *OH to $\text{*H}_2\text{O}$ and desorption of $\text{*H}_2\text{O}$. Similarly, in systems with Ir, *CO follows the same reduction pathway, with *OH on Si being preferentially hydrogenated to $\text{*H}_2\text{O}$. The $\text{*CH}_2\text{OH}$ is then converted to CH_4 via the sequence $\text{*CH}_2\text{OH} \rightarrow \text{*CH}_2 + \text{*OH} \rightarrow \text{*CH}_3 + \text{*OH} \rightarrow \text{*OH} + \text{CH}_4$. Subsequently, *OH is hydrogenated to $\text{*H}_2\text{O}$ and then desorbed.

In systems incorporating late transition metals (Ni, Pd, Pt, Cu, Ag, Au, Zn, Cd), the SiTM DACs predominantly facilitate the formation of the vertical *OCHO intermediate. Among them, one O of *OCHO only bonds with Si. This intermediate is subsequently reduced to CH_4 through the pathway: $\text{*OCHO} \rightarrow \text{*HCOOH} \rightarrow \text{*OCH}_2\text{OH} \rightarrow \text{*OCH}_2\text{OH}_2 \rightarrow \text{*CH}_2\text{O} \rightarrow \text{*OCH}_3 \rightarrow \text{*O} + \text{CH}_4$. Following this pathway, *O is initially hydrogenated to *OH , which is then further hydrogenated to $\text{*H}_2\text{O}$ prior to desorption.

Interestingly, despite these differences, CH_3OH or CH_4 , the multi-electron transfer product, emerged as the most favored product in all cases. The Gibbs free energy change in the most basic step of CO_2 reduction on SiTM DAC is more favorable than that on traditional TM DACs, especially the energy change from *CO to *CHO is significantly reduced, which allows *CO to be further reduced into multi-electron transfer products. However, the high positive charge carried by Si complicates the desorption of *OH , making the $\text{*OH} \rightarrow \text{*H}_2\text{O}$ transition the potential-determining step, as summarized in Table S3.† Si atoms are easily occupied by *OH in most cases. And *OH is an intermediate in all pathways, indicating the importance of *OH in CO_2RR . As shown in the Fig. 3(b), among the 27 SiTMN₆ DACs, seven of them (Co, Ni, Y, Rh, Pd, Ir, Pt) exhibit lower ΔG_{max} characteristics than SiFeN₆, indicating that these structures have higher activity in CO_2RR .

We also explored the competitive relationship between the CO_2RR and the hydrogen evolution reaction (HER), as illustrated in Fig. S21.† In all cases, SiTMN₆ structures demonstrated a preference for CO_2RR . Additionally, we examined the competitive adsorption of *H , $\text{*H}_2\text{O}$, and *CO_2 . *H and $\text{*H}_2\text{O}$ are predominantly adsorbed at the Si sites, whereas *CO_2 is bound to both Si and TM atoms. This differential adsorption

behavior suggests that the *H and $\text{*H}_2\text{O}$ adsorptions have less influence on TM atoms, compared to that of *CO_2 . As shown in Fig. S22,† $\Delta G_{\text{*H}_2\text{O}} - \Delta G_{\text{*CO}_2}$ and $\Delta G_{\text{*H}} - \Delta G_{\text{*CO}_2}$ are linearly correlated with $\Delta G_{\text{*CO}_2}$. Enhanced CO_2 adsorption facilitates the progression of CO_2RR , making the pairing of middle TM atoms with Si particularly advantageous. According to the fitting results, when $\Delta G_{\text{*CO}_2}$ is less than -0.96 eV, SiTM DACs will have stronger adsorption interactions with *CO_2 , compared to *H and $\text{*H}_2\text{O}$. Therefore, among the 7 SiTM DACs with ΔG_{max} lower than SiFeN₆, the SiCoN₆, SiRhN₆ and SiIrN₆ DACs are more likely to exhibit superior CO_2RR performance. Furthermore, we calculated the dissolution potentials for the SiCoN₆, SiRhN₆, and SiIrN₆ DACs, finding that all values exceeded 0 V, as shown in Table S4.† This suggests that these structures are stable under electrochemical conditions.

3.4 Exploration of universal descriptors for SiTMN₆ DACs

In general, the catalytic descriptors are invaluable tools for evaluating performance and guiding the design of highly active catalysts. Here we have systematically analyzed several general descriptors to gauge the reactivity of reactants on various SiTMN₆ DACs.

Firstly, for a series of same reactions or intermediates, their free energy changes often exhibit linear correlations due to their similar interactions in chemical environments and active sites. Accordingly, we employed the similar descriptor $\Delta G_{\text{*OH}}$ to describe the catalytic behavior of CO_2RR on SiTMN₆ DACs. Selection of descriptor is based on the fact that PDS occurs mainly in $\text{*OH} \rightarrow \text{*H}_2\text{O}$. We found a linear relationship between $\Delta G_{\text{*OH}}$ and ΔG_{max} (Fig. 4(a)). And there is a tendency that ΔG_{max} is too high when $N_c = 2$, and the ΔG_{max} is relatively low when $N_c = 3$. The production of $\text{*H}_2\text{O}$ from *OH species is challenging to achieve due to the strong combination of *OH species, resulting in the $\text{*OH} \rightarrow \text{*H}_2\text{O}$ production as the PDS. Consequently, the appropriate reduction of the $\Delta G_{\text{*OH}}$ through

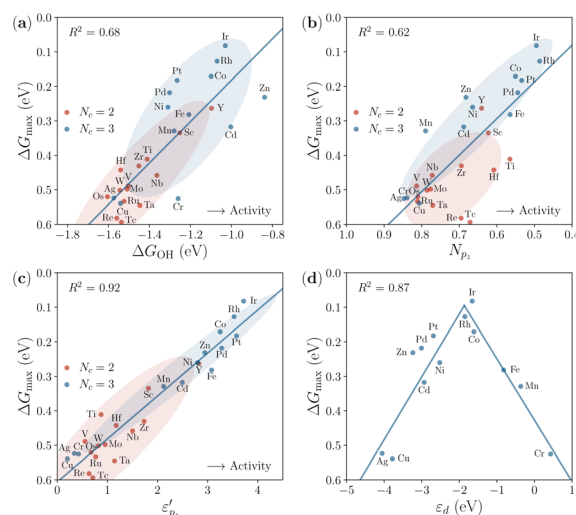


Fig. 4 Correlations between (a) $\Delta G_{\text{*OH}}$, (b) N_{p_c} , (c) ϵ'_{p_c} and (d) ϵ_d and ΔG_{max} of SiTMN₆ DACs.

adjustment of the electronic structure enables to acquire superior active catalysts.

However, what is the key factor that affects the ΔG_{*OH} ? Considering the interaction between SiTMN₆ DACs and reaction intermediates, notably *OH and *H₂O, primarily adsorbed on the top of Si. Further investigation explored the relationship between the electronic properties of Si and reaction activity. We initially correlated the number of p_z electrons (N_{p_z}) with ΔG_{max} . As illustrated in Fig. 4(b), as N_{p_z} decreases, the ΔG_{max} decreases. This is due to a larger N_{p_z} leading to more electron interaction with the O atom in *OH. However, N_{p_z} in Si atoms only shows a weak linear correlation with ΔG_{max} . This indicates that the N_{p_z} in Si atoms are insufficient for describing the CO₂RR activity. We then explored the p_z distribution of Si atoms, which is represented by the p_z band distribution (ϵ'_{p_z}). As shown in Fig. 4(c), the ϵ'_{p_z} of Si atoms exhibits a significant linear correlation with ΔG_{max} . The smaller the ϵ'_{p_z} , the higher the ΔG_{max} . Similarly to ΔG_{*OH} , when $N_c = 3$, there are smaller N_{p_z} and larger ϵ'_{p_z} . Additionally, while *OH is adsorbed at the top site of Si in various SiTM DACs, the capacity for *OH adsorption varies depending on the associated TM atoms.

To investigate the interactions between the Si atom and *OH, as well as between the Si atom and the TM atom, we analyze PDOS for these systems. Here two characteristics can be found: (i) as exemplified with SiCrN₆, SiIrN₆, SiAgN₆ and Si₂N₆ DACs in Fig. S23,† the $\Delta G_{*OH \rightarrow *H_2O}$ values of these structures are 0.52, 0.08, 0.53, and 0.35 eV, respectively. We found that the TM d-orbitals regulate the distribution of p_z orbitals of Si through the p–d coupling. Notably, the d electron distribution of Cr is closest to the Fermi level, resulting in optimal alignment with Si p_z electrons and the most robust p–d coupling. This alignment induces pronounced electron occupation and unoccupied states in Si p_z near the Fermi level. Conversely, as the d electron distribution shifts downward (SiIrN₆), the strength of this coupling effect reduces, where strong p_z electron occupancy is absent. Intriguingly, as the d electron distribution shifts further downward (in the case of SiAgN₆), a pronounced p–d hybridization peak reemerges below the Fermi level. The proximity of p_z electrons to the Fermi level enhances electron transfer from Si to *OH, resulting in increased *OH adsorption. Additionally, prior to adsorption, the SiIrN₆ structures exhibited significantly lower number of p_z electrons compared to the other configurations, effectively reducing Si–OH interactions. After adsorption, the other three structures showed a substantial transfer of p_z electrons to *OH. This suggests a trend characterized by an optimal d band distribution, complemented by a suitable p_z band distribution and a reduced ΔG_{max} . (ii) As exemplified with SiFeN₆, SiRuN₆ and SiOsN₆ DACs in Fig. S24,† the $\Delta G_{*OH \rightarrow *H_2O}$ values of these structures are 0.28, 0.53 and 0.52 eV, respectively. We have discovered that an increase in the coordination number of nitrogen can decrease the p_z electrons in Si atom, raising the ϵ'_{p_z} larger, thereby decreasing the reactive activity of Si. Specifically, the Fe, Ru, and Os exhibit a closely related d electron distribution. However, the corresponding p_z electron counts are 0.56, 0.78, and 0.78, respectively. And p_z electron distribution as a whole move upwards, away from the Fermi level. Therefore, this results in a lower ΔG_{max} for SiFeN₆ DACs

compared to SiRuN₆ and SiOsN₆ DACs. This phenomenon is primarily attributed to the more suitable radius of Fe compared to other elements, which allows the Si atom to form stronger bonds with three coordinated nitrogen atoms on the graphene surface, thus affecting its chemical activity. These trends correlate with the ϵ'_{p_z} , as detailed in Fig. S6(a).† The data is categorized into two groups, $N_c = 2$ and $N_c = 3$, with a linear and volcanic correlation between ϵ_d and ϵ'_{p_z} , respectively. Similar distinct grouping patterns are also found for the relation between ϵ_d of TM atoms and ΔG_{max} , as shown in Fig. S6(b).† Specifically, as shown in Fig. 4(d), when $N_c = 3$, ϵ_d values of TM atoms and ΔG_{max} exhibit a volcanic relationship. The optimal catalytic activity of DACs is observed when Si is combined with Co, Rh, or Ir. Both excessively deep and shallow ϵ_d energy levels can lead to suboptimal p–d coupling, causing a gradually decrease of ϵ'_{p_z} . This decrease complicates the protonation of *OH, resulting in an excessively large ΔG_{max} . These findings highlight the significant role of Si p_z electronic properties in tuning catalytic activity of DACs, which are influenced by both p–d orbital coupling and the coordinating atoms. This insight opens up an avenue for the rational design of DACs through electron regulation of the dual-atom active site and its interface environment.

3.5 Exploration of SiTMN₅An DACs for CO₂RR

Our findings illustrate that CO₂RR activity of SiTMN₆ DACs can be effectively modulated by adjusting the p_z electron distribution in silicon atoms. Since the coordination environment also has an impact on the diatomic center, the chemical modification of the N₆ coordination environment was also considered here. Carbon (C) is an intrinsic defect and boron (B) can create an electron-deficient environment to suppress the activity of Si. Therefore, we decided to replace the N atom with the common coordination atoms B and C. Considering the unequivalence at different positions, we have adjusted 6 N atoms closest to Si and TM atoms, thereby expanding the catalyst space to 336 SiTMN₅An DACs. In order to ensure the diversity of the dataset as much as possible, Au is still retained in this stage.

We consider a first round of high-throughput screening of these materials for their catalytic activity and selectivity by using ΔG_{*CO_2} and ΔG_{*OH} . This is because sufficient *CO₂ adsorption capacity ensures the progress of CO₂RR, and the adsorption capacity of *OH reflects the activity of CO₂RR. The acquisition of ΔG_{*CO_2} and ΔG_{*OH} is accelerated by machine learning. The efficacy of the machine learning approach in our study is highlighted by the results depicted in Fig. 5(a and b). Both models demonstrated excellent predictive accuracy with R^2 scores of 0.90 across training and test datasets, underscoring the robustness of the machine learning algorithms employed. This high level of performance confirms the reliability of using the optimal feature set derived from our analysis to predict the desired properties of catalysts within the prediction set.

Fig. 5(c and d) provides a visual representation of the feature importance for ΔG_{*CO_2} and ΔG_{*OH} . Detailed feature descriptions are shown in Table S2.† The features identified through the feature engineering process are largely consistent with

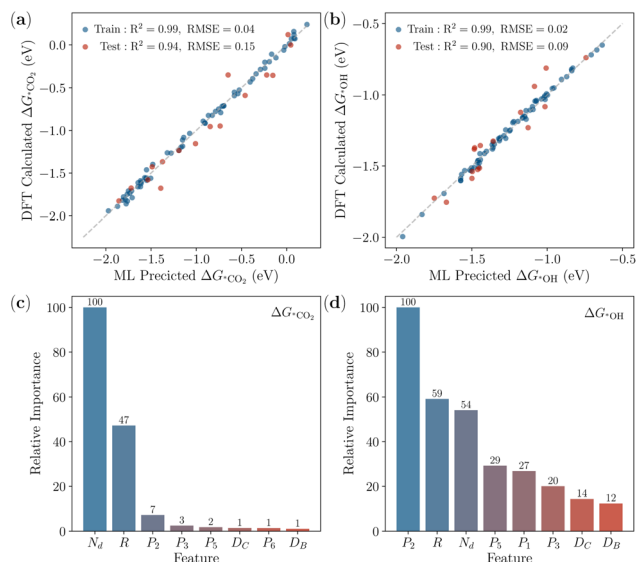


Fig. 5 Machine learning training results based on GBR of SiTMN₅An DACs for (a) $\Delta G^*_{\text{CO}_2}$ and (b) ΔG^*_{OH} . Calculated feature importance based on GBR of SiTMN₅An DACs for (c) $\Delta G^*_{\text{CO}_2}$ and (d) ΔG^*_{OH} .

established theoretical understandings. Primarily, the number of d electrons (N_d) in the TM atoms and the atomic radius (R) of these TM atoms have been recognized to be critical in influencing both $\Delta G^*_{\text{CO}_2}$ and ΔG^*_{OH} . Notably, N_d emerges as the most influential factor in determining $\Delta G^*_{\text{CO}_2}$, underscoring the primary role of d electron in the interaction between TM atoms and CO₂ molecules. Moderate counts of d electrons are found to facilitate the strongest CO₂ adsorption, indicating that either an excess or a deficiency of d electrons is weak adsorption. Such d electron population balance ensures that sufficient electrons are available to donate to the LUMO orbitals of CO₂, while also providing enough empty orbitals to accept electrons from the CO₂ HOMO orbitals, as shown in the Fig. S26.† Furthermore, d electrons significantly impact *OH adsorption by modulating the p_z electron distribution in Si, which in turn affects *OH adsorption. The radius of TM atoms also plays a crucial role by influencing the structure and thereby altering the adsorption energy. This modulation primarily affects the bonding state at the SiTM active site with its coordination environment. Interestingly, while features related to the coordination environment generally exhibited lower importance in the training for $\Delta G^*_{\text{CO}_2}$, they were highly significant in predicting ΔG^*_{OH} . Among these, P_2 (doping of position 2) emerged as a critical factor, highlighting the substantial impact that changes in the coordination environment can have on the adsorption characteristics of *OH.

Subsequently, We employed these models to predict $\Delta G^*_{\text{CO}_2}$ and ΔG^*_{OH} values for remaining configurations and conducted a targeted screening based on these predictions. By incorporating a diverse set of TM atoms and coordination environments, this model enables us to make predictions within minutes, significantly accelerating the screening process. To ensure the selection of catalysts with optimal reaction selectivity, activity and the prediction error, we established specific screening thresholds: $\Delta G^*_{\text{CO}_2}$ was set to be less than -0.87 eV,

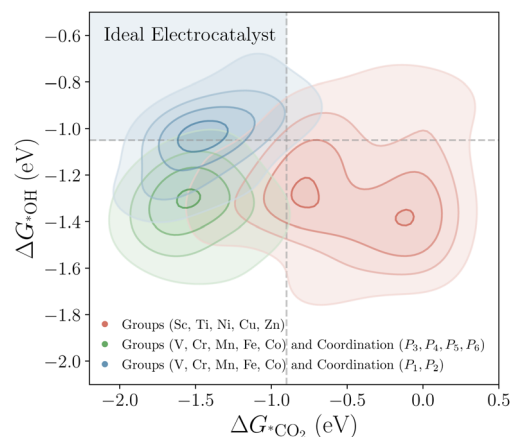


Fig. 6 Density contour plots of $\Delta G^*_{\text{CO}_2}$ and ΔG^*_{OH} for different SiTMN₅An DACs.

and ΔG^*_{OH} was required to be less than -1.05 eV. Fig. 6 and S27† depict that elements such as Sc, Ti, Ni, Cu, and Zn demonstrated weak CO₂ adsorption capacities, rendering them less favorable for CO₂ reduction. Further screening highlighted that modifying the coordination atoms directly bonded to Si, particularly the N atoms at positions 1 and 2, could effectively lower ΔG^*_{OH} .

After applying these criteria, 33 structures remained eligible for further analysis, as detailed in Table S5.† We then conducted DFT calculations on these structures to refine the selection based on $\Delta G^*_{\text{OH} \rightarrow *H_2O}$, identifying 6 potential catalysts with $\Delta G^*_{\text{OH} \rightarrow *H_2O}$ values below 0 eV. Ultimately, the screening process predominantly selected structures involving Si and Co, Rh, Ir, with a preference for configurations where N atom at position 2 was replaced. This refined set of candidates demonstrates the potential for high catalytic activity in CO₂RR. DFT validations were conducted on these six screened catalysts, with the corresponding free energy step diagrams detailed in Fig. S28–S30.† The ΔG_{max} , products and PDS for these structures are summarized in Table 1. The ΔG_{max} of these structures ranged from -0.06 to 0.05 eV, indicating that the SiTMN₅An DACs are highly active for CO₂RR. In addition, we calculated the dissolution potentials of these structures and found that they were all above 0 V, as detailed in Table S4,† indicating that these structures are stable under electrochemical conditions.

Additionally, the linear relationships between ΔG^*_{OH} and ΔG_{max} , and between ϵ'_{P_2} and ΔG_{max} , remain valid after

Table 1 Final screening results of SiTMN₅An. SiTMN₅An is abbreviated as TMAN

Structure	ΔG_{max}	Product	Potential-determining step
CoB2	-0.05	CH ₄	*CO + *OH → *CO + *H ₂ O
CoC2	0.03	CH ₄	*CO + *OH → *CHO + *OH
RhB2	-0.06	CH ₄	*CHO + *OH → *CHO + *H ₂ O
RhC2	0.05	CH ₃ OH	*CHO + *OH → *CHOH + *OH
IrB2	0.03	CH ₄	*CO + *OH → *CHO + *OH
IrC2	-0.01	CH ₄	*CO + *OH → *CHO + *OH

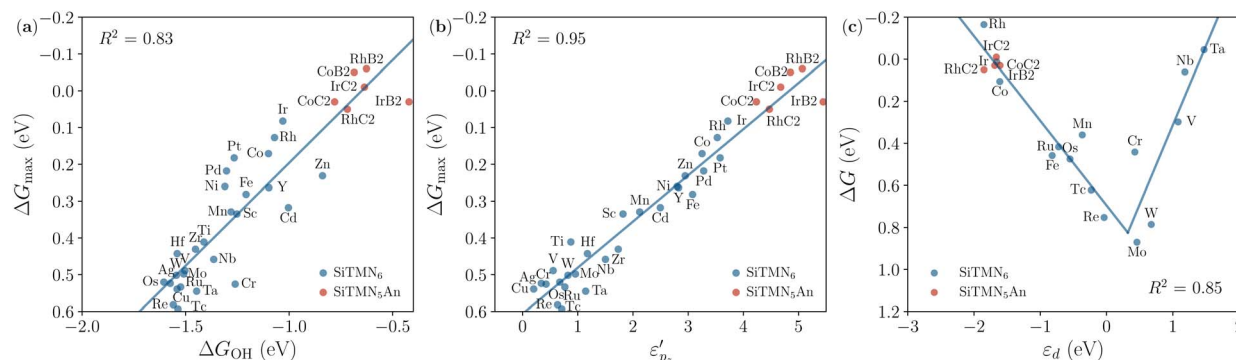


Fig. 7 Correlations between (a) ΔG_{max} , (b) ϵ'_{p_z} and ΔG_{max} of SiTMN₆ and screened SiTMN₅An DACs; (c) correlations between ΔG for $^*\text{CO} + ^*\text{OH} \rightarrow ^*\text{CHO} + ^*\text{OH}$ and ϵ_d on SiTMN₆ DACs and ΔG_{max} and ϵ_d on screened SiTMN₅An DACs.

considering these new structures, as illustrated in Fig. 7(a and b). This proves that our strategy is effective. However, N_{p_z} in Si atoms does not exhibit linear relationship with ΔG_{max} , as shown in Fig. S31.† This observation suggests that modifications in the coordination environment do not significantly alter the electron transfer capabilities of Si atoms. Instead, these changes primarily influence catalytic activity by adjusting the p_z electron distribution in Si.

Actually, the transformation of $^*\text{OH} \rightarrow ^*\text{H}_2\text{O}$ no longer limits the entire reaction process due to effective regulation of the coordination environment. For some of the new structures, the PDS is no longer $^*\text{OH} \rightarrow ^*\text{H}_2\text{O}$ but shifts to $^*\text{CO} \rightarrow ^*\text{CHO}$ or $^*\text{CHO} \rightarrow ^*\text{CHOH}$, predominantly occurring on TM atoms. In addition to ΔG_{max} for SiCoN₅C₂, SiRhN₅C₂, SiIrN₅B₂ and SiIrN₅C₂ DACs, we considered the ΔG for $^*\text{CO} + ^*\text{OH} \rightarrow ^*\text{CHO} + ^*\text{OH}$ on SiTMN₆ DACs. As illustrated in Fig. 7(c), the relationship between the ΔG and ϵ_d is an inversely volcanic correlation, indicating that the closer proximity the ϵ_d to the Fermi level, the higher the ΔG . Co, Rh, and Ir have the most suitable d band center, aligning with the ΔG values for this reaction, thus indicating that SiCo, SiRh, and SiIr DACs exhibit optimal activity. Overall, our strategy effectively reduces $\Delta G_{^*\text{OH}}$ by adjusting the p_z electron distribution in Si, thereby enhancing the catalysts' activity.

4 Conclusions

In summary, the catalytic performance of SiTM DACs for CO₂RR was systematically investigated through DFT calculations and machine learning. It was revealed that the superior activity of SiTM DACs primarily originates from the exceptional catalytic capabilities of the Si atoms, which enhance the adsorption and activation of key reactants. Importantly, the synergistic interaction within the SiTM framework effectively enhances the stabilization of the $^*\text{CHO}$, facilitating the conversion to multi-electron transfer products.

Of all tested SiTM DACs configurations, those incorporating VIII transition metals (Co, Rh, and Ir) in conjunction with Si exhibited the highest catalytic performance. Therefore, these elements should be prioritized when synthesizing high-activity SiTM DACs for CO₂RR applications. The adsorption free energy

of $^*\text{OH}$, along with the ϵ'_{p_z} of Si atoms, emerged as critical descriptors for gauging catalytic performance.

Furthermore, modifications to the coordination environment through B and C substitution were explored *via* high-throughput screening of 336 potential structures of DACs, revealing that B or C substitution at the secondary nitrogen position significantly enhances the catalytic activity by modulating the p_z electron distribution in Si. This insight into structural and electronic descriptors emphasizes their importance in elucidating the activity regulation mechanisms of SiTM DACs for CO₂RR and paves the way for novel design strategies in dual-atom catalysis.

Data availability

The authors declare that the data supporting the findings of this article have been included as part of the ESI.† The version of scikit-learn employed for this study is version 1.3.0. Additional relevant data are available from the corresponding authors upon reasonable request.

Author contributions

Meijie Wang: investigation, data curation, writing-original draft, visualization. Yaowei Xiang and Yuxing Lin: formal analysis. Yang Sun, Shunqing Wu and Zi-Zhong Zhu: writing-review & editing. Xinrui Cao: conceptualization, supervision, writing-review & editing.

Conflicts of interest

There are no conflicts to declare.

Acknowledgements

This work is supported by National Natural Science Foundation of China (22073076 and 21933009), and the Fundamental Research Funds for the Central Universities of China (20720210023 and 20720240138). The Xiamen University's High-Performance Computing Center and the State Key Laboratory Chemistry of Solid Surfaces at the Xiamen University are

acknowledged for the supercomputer resources. Shaorong Fang and Tianfu Wu from Information and Network Center of Xiamen University are acknowledged for the help with the GPU computing.

References

- N. S. Lewis and D. G. Nocera, *Proc. Natl. Acad. Sci. U. S. A.*, 2006, **103**, 15729–15735.
- S. J. Davis, K. Caldeira and H. D. Matthews, *Science*, 2010, **329**, 1330–1333.
- R. A. Betts, O. Boucher, M. Collins, P. M. Cox, P. D. Falloon, N. Gedney, D. L. Hemming, C. Huntingford, C. D. Jones, D. M. H. Sexton and M. J. Webb, *Nature*, 2007, **448**, 1037–1041.
- R. Francke, B. Schille and M. Roemelt, *Chem. Rev.*, 2018, **118**, 4631–4701.
- J. Wu, T. Sharifi, Y. Gao, T. Zhang and P. M. Ajayan, *Adv. Mater.*, 2019, **31**, 1804257.
- M. Li, H. Wang, W. Luo, P. C. Sherrell, J. Chen and J. Yang, *Adv. Mater.*, 2020, **32**, 2001848.
- H. Zhang, J. Li, S. Xi, Y. Du, X. Hai, J. Wang, H. Xu, G. Wu, J. Zhang, J. Lu and J. Wang, *Angew. Chem., Int. Ed.*, 2019, **58**, 14871–14876.
- F. Pan, H. Zhang, K. Liu, D. Cullen, K. More, M. Wang, Z. Feng, G. Wang, G. Wu and Y. Li, *ACS Catal.*, 2018, **8**, 3116–3122.
- H. B. Yang, S.-F. Hung, S. Liu, K. Yuan, S. Miao, L. Zhang, X. Huang, H.-Y. Wang, W. Cai, R. Chen, J. Gao, X. Yang, W. Chen, Y. Huang, H. M. Chen, C. M. Li, T. Zhang and B. Liu, *Nat. Energy*, 2018, **3**, 140–147.
- P. Brimley, H. Almajed, Y. Alsunni, A. W. Alherz, Z. J. L. Bare, W. A. Smith and C. B. Musgrave, *ACS Catal.*, 2022, **12**, 10161–10171.
- Y. Wang, J. Mao, X. Meng, L. Yu, D. Deng and X. Bao, *Chem. Rev.*, 2019, **119**, 1806–1854.
- L. Li, K. Yuan and Y. Chen, *Acc. Mater. Res.*, 2022, **3**, 584–596.
- M. Ren, X. Guo, S. Zhang and S. Huang, *Adv. Funct. Mater.*, 2023, **33**, 2213543.
- S. De, A. Dokania, A. Ramirez and J. Gascon, *ACS Catal.*, 2020, **10**, 14147–14185.
- W. Zhang, D. Ma, J. Pérez-Ramírez and Z. Chen, *Adv. Energy Sustainability Res.*, 2022, **3**, 2100169.
- S. Jin, Z. Hao, K. Zhang, Z. Yan and J. Chen, *Angew. Chem., Int. Ed.*, 2021, **60**, 20627–20648.
- W. Zhang, Y. Chao, W. Zhang, J. Zhou, F. Lv, K. Wang, F. Lin, H. Luo, J. Li, M. Tong, E. Wang and S. Guo, *Adv. Mater.*, 2021, **33**, 2102576.
- Y. Hu, Z. Li, B. Li and C. Yu, *Small*, 2022, **18**, 2203589.
- R. Li and D. Wang, *Adv. Energy Mater.*, 2022, **12**, 2103564.
- W. Ren, X. Tan, W. Yang, C. Jia, S. Xu, K. Wang, S. C. Smith and C. Zhao, *Angew. Chem., Int. Ed.*, 2019, **58**, 6972–6976.
- H. Cheng, X. Wu, M. Feng, X. Li, G. Lei, Z. Fan, D. Pan, F. Cui and G. He, *ACS Catal.*, 2021, **11**, 12673–12681.
- J.-d. Yi, X. Gao, H. Zhou, W. Chen and Y. Wu, *Angew. Chem.*, 2022, **134**, e202212329.
- Q. Hao, H.-x. Zhong, J.-z. Wang, K.-h. Liu, J.-m. Yan, Z.-h. Ren, N. Zhou, X. Zhao, H. Zhang, D.-x. Liu, X. Liu, L.-w. Chen, J. Luo and X.-b. Zhang, *Nat. Synth.*, 2022, **1**, 719–728.
- J. Zhu, M. Xiao, D. Ren, R. Gao, X. Liu, Z. Zhang, D. Luo, W. Xing, D. Su, A. Yu and Z. Chen, *J. Am. Chem. Soc.*, 2022, **144**, 9661–9671.
- Z. Zeng, L. Y. Gan, H. Bin Yang, X. Su, J. Gao, W. Liu, H. Matsumoto, J. Gong, J. Zhang, W. Cai, Z. Zhang, Y. Yan, B. Liu and P. Chen, *Nat. Commun.*, 2021, **12**, 4088.
- Y. Li, W. Shan, M. J. Zachman, M. Wang, S. Hwang, H. Tabassum, J. Yang, X. Yang, S. Karakalos, Z. Feng, G. Wang and G. Wu, *Angew. Chem., Int. Ed.*, 2022, **61**, e202205632.
- X. Zhao, K. Zhao, Y. Liu, Y. Su, S. Chen, H. Yu and X. Quan, *ACS Catal.*, 2022, **12**, 11412–11420.
- L. Zhang, J. Feng, S. Liu, X. Tan, L. Wu, S. Jia, L. Xu, X. Ma, X. Song, J. Ma, X. Sun and B. Han, *Adv. Mater.*, 2023, **35**, 2209590.
- Y. Li, B. Wei, M. Zhu, J. Chen, Q. Jiang, B. Yang, Y. Hou, L. Lei, Z. Li, R. Zhang and Y. Lu, *Adv. Mater.*, 2021, **33**, 2102212.
- X. Wei, S. Wei, S. Cao, Y. Hu, S. Zhou, S. Liu, Z. Wang and X. Lu, *Appl. Surf. Sci.*, 2021, **564**, 150423.
- S. Wang, L. Li, J. Li, C. Yuan, Y. Kang, K. S. Hui, J. Zhang, F. Bin, X. Fan, F. Chen and K. N. Hui, *J. Phys. Chem. C*, 2021, **125**, 7155–7165.
- Y. Ouyang, L. Shi, X. Bai, Q. Li and J. Wang, *Chem. Sci.*, 2020, **11**, 1807–1813.
- S. Cao, S. Zhou, H. Chen, S. Wei, S. Liu, X. Lin, X. Chen, Z. Wang, W. Guo and X. Lu, *Energy Environ. Mater.*, 2023, **6**, e12287.
- H. Chen, Q. Wu, Y. Wang, Q. Zhao, X. Ai, Y. Shen and X. Zou, *Chem. Commun.*, 2022, **58**, 7730–7740.
- P. Li, J. Bi, J. Liu, Y. Wang, X. Kang, X. Sun, J. Zhang, Z. Liu, Q. Zhu and B. Han, *J. Am. Chem. Soc.*, 2023, **145**, 4675–4682.
- W.-F. Xiong, D.-H. Si, H.-F. Li, X. Song, T. Wang, Y.-B. Huang, T.-F. Liu, T. Zhang and R. Cao, *J. Am. Chem. Soc.*, 2024, **146**, 289–297.
- M. Wang, Y. Xiang, W. Chen, S. Wu, Z.-Z. Zhu and X. Cao, *Appl. Surf. Sci.*, 2024, **643**, 158724.
- W. Xie, H. Li, G. Cui, J. Li, Y. Song, S. Li, X. Zhang, J. Y. Lee, M. Shao and M. Wei, *Angew. Chem., Int. Ed.*, 2021, **60**, 7382–7388.
- H. S. Kim, C. H. Lee, J.-H. Jang, M. S. Kang, H. Jin, K.-S. Lee, S. U. Lee, S. J. Yoo and W. C. Yoo, *J. Mater. Chem. A*, 2021, **9**, 4297–4309.
- R. Qin, K. Liu, Q. Wu and N. Zheng, *Chem. Rev.*, 2020, **120**, 11810–11899.
- J. Wang, H. Li, S. Liu, Y. Hu, J. Zhang, M. Xia, Y. Hou, J. Tse, J. Zhang and Y. Zhao, *Angew. Chem., Int. Ed.*, 2021, **60**, 181–185.
- Z. Qi, Y. Zhou, R. Guan, Y. Fu and J.-B. Baek, *Adv. Mater.*, 2023, **35**, 2210575.
- J. Zhang, H. Yang and B. Liu, *Adv. Energy Mater.*, 2021, **11**, 2002473.

- 44 F. Wang, R. Zhang, Y. Zhang, Y. Li, J. Zhang, W. Yuan, H. Liu, F. Wang and H. L. Xin, *Adv. Funct. Mater.*, 2023, **33**, 2213863.
- 45 Y.-N. Gong, C.-Y. Cao, W.-J. Shi, J.-H. Zhang, J.-H. Deng, T.-B. Lu and D.-C. Zhong, *Angew. Chem., Int. Ed.*, 2022, **61**, e202215187.
- 46 J. Wu, D. Wu, H. Li, Y. Song, W. Lv, X. Yu and D. Ma, *Nanoscale*, 2023, **15**, 16056–16067.
- 47 Q. Dang, S. Tang, T. Liu, X. Li, X. Wang, W. Zhong, Y. Luo and J. Jiang, *J. Phys. Chem. Lett.*, 2021, **12**, 8355–8362.
- 48 Y. Zhang, X. Wang, T. Liu, Q. Dang, L. Zhu, Y. Luo, J. Jiang and S. Tang, *J. Mater. Chem. A*, 2022, **10**, 23704–23711.
- 49 Y. Zhang, D. Wang, G. Wei, B. Li, Z. Mao, S.-M. Xu, S. Tang, J. Jiang, Z. Li, X. Wang and X. Xu, *JACS Au*, 2024, **4**(4), 1509–1520.
- 50 G. Kresse and J. Furthmüller, *Phys. Rev. B: Condens. Matter Mater. Phys.*, 1996, **54**, 11169–11186.
- 51 G. Kresse and J. Furthmüller, *Comput. Mater. Sci.*, 1996, **6**, 15–50.
- 52 P. E. Blöchl, *Phys. Rev. B: Condens. Matter Mater. Phys.*, 1994, **50**, 17953–17979.
- 53 J. P. Perdew, K. Burke and M. Ernzerhof, *Phys. Rev. Lett.*, 1996, **77**, 3865–3868.
- 54 S. Grimme, J. Antony, S. Ehrlich and H. Krieg, *J. Chem. Phys.*, 2010, **132**, 154104.
- 55 S. Grimme, S. Ehrlich and L. Goerigk, *J. Comput. Chem.*, 2011, **32**, 1456–1465.
- 56 V. Wang, N. Xu, J.-C. Liu, G. Tang and W.-T. Geng, *Comput. Phys. Commun.*, 2021, **267**, 108033.
- 57 R. Sundararaman, K. Letchworth-Weaver, K. A. Schwarz, D. Gunceler, Y. Ozhabes and T. Arias, *SoftwareX*, 2017, **6**, 278–284.
- 58 D. Kim, J. Shi and Y. Liu, *J. Am. Chem. Soc.*, 2018, **140**, 9127–9131.
- 59 K. F. Garrity, J. W. Bennett, K. M. Rabe and D. Vanderbilt, *Comput. Mater. Sci.*, 2014, **81**, 446–452.
- 60 X. Guo, J. Gu, S. Lin, S. Zhang, Z. Chen and S. Huang, *J. Am. Chem. Soc.*, 2020, **142**, 5709–5721.
- 61 J. H. Friedman, *Ann. Stat.*, 2001, **29**, 1189.
- 62 S. Zhang, S. Lu, P. Zhang, J. Tian, L. Shi, C. Ling, Q. Zhou and J. Wang, *Energy Environ. Mater.*, 2023, **6**, e12304.
- 63 T. Yang, D. Zhou, S. Ye, X. Li, H. Li, Y. Feng, Z. Jiang, L. Yang, K. Ye, Y. Shen, S. Jiang, S. Feng, G. Zhang, Y. Huang, S. Wang and J. Jiang, *J. Am. Chem. Soc.*, 2023, **145**, 26817–26823.
- 64 Y. Jiao, H. Li, Y. Jiao and S.-Z. Qiao, *J. Am. Chem. Soc.*, 2023, **145**, 15572–15580.
- 65 W. Li, G. Feng, S. Wang, X. Zhong, Z. Yao, S. Deng and J. Wang, *J. Mater. Chem. A*, 2023, **11**, 15426–15436.
- 66 Z. Wang, Y. Gong, M. L. Evans, Y. Yan, S. Wang, N. Miao, R. Zheng, G.-M. Rignanese and J. Wang, *J. Am. Chem. Soc.*, 2023, **145**, 26412–26424.
- 67 Y.-C. Gao, N. Yao, X. Chen, L. Yu, R. Zhang and Q. Zhang, *J. Am. Chem. Soc.*, 2023, **145**, 23764–23770.
- 68 Q. Ye, X. Yi, C.-Z. Wang, T. Zhang, Y. Liu, S. Lin and H. J. Fan, *Adv. Funct. Mater.*, 2024, **34**, 2400107.
- 69 F. Pedregosa, G. Varoquaux, A. Gramfort, V. Michel, B. Thirion, O. Grisel, M. Blondel, P. Prettenhofer, R. Weiss, V. Dubourg, J. Vanderplas, A. Passos, D. Cournapeau, M. Brucher, M. Perrot and E. Duchesnay, *J. Mach. Learn. Res.*, 2011, **12**, 2825–2830.